ELSEVIER

Contents lists available at ScienceDirect

Journal of Neuroscience Methods

journal homepage: www.elsevier.com/locate/jneumeth





An approach for in-situ detection of gold colloid aggregates amyloid formations within the hippocampus of the Cohen's Alzheimer's disease rat model by surface enhanced raman scattering methods

Kazushige Yokoyama a,* , Joshua Thomas a , Windsor Ardner a , Madison Kieft a , Lorenz S. Neuwirth b,c , Wei Liu d

- ^a Department of Chemistry, The State University of New York Geneseo College, Geneseo, NY, USA
- ^b Department of Psychology, The State University of New York Old Westbury, Old Westbury, NY, USA
- ^c SUNY Neuroscience Research Institute, The State University of New York Old Westbury, Old Westbury, NY, USA
- ^d WITec Instruments Corp, Knoxville, TN, USA

ARTICLE INFO

Keywords: Alzheimer's disease (AD) Cohen's Alzheimer's disease model Surface plasmon Surface Enhanced Raman Scattering (SERS) Gold nano-particles Protein corona

ABSTRACT

Background: Amyloid beta $(A\beta)$ peptides, such as $A\beta_{1-40}$ or $A\beta_{1-42}$ are regarded as hallmark neuropathological biomarkers associated with Alzheimer's disease (AD). The formation of an aggregates by $A\beta_{1-40}$ or $A\beta_{1-42}$ -coated gold nano-particles are hypothesized to contain conformation of $A\beta$ oligomers, which could exist only at an initial stage of fibrillogenesis.

New Method: The attempt of in-situ detection of externally initiated gold colloid (ca. 80 nm diameter) aggregates in the middle section of the hippocampus of the Long Evans Cohen's Alzheimer's disease rat model was conducted through the Surface Enhanced Raman Scattering (SERS) method.

Results: The SERS spectral features contained modes associated with β -sheet interactions and a significant number of modes that were previously reported in SERS shifts for Alzheimer diseased rodent and human brain tissues; thereby, strongly implying a containment of amyloid fibrils. The spectral patterns were further examined and compared with those collected from *in-vitro* gold colloid aggregates which were formed from $A\beta_{1-40}$ - or $A\beta_{1-42}$ -coated 80 nm gold colloid under pH \sim 4, pH \sim 7, and pH \sim 10, and the best matched datasets were found with that of the aggregates of $A\beta_{1-42}$ -coated 80 nm gold colloid at \sim pH 4.0. The morphology and physical size of this specific gold colloid aggregate was clearly different from those found *in-vitro*.

Comparison with Existing Method(s): The amyloid fibril with a β -sheet conformation identified in previously reported in AD mouse/human brain tissues was involved in a formation of the gold colloid aggregates. However, to our surprise, best explanation for the observed SERS spectral features was possible with those in vitro $A\beta_{1-42}$ -coated 80 nm gold colloid under pH \sim 4.

Conclusions: A formation of gold colloid aggregates was confirmed in the AD rat hippocampal brain section with unique physical morphology compared to those observed in *in-vitro* $A\beta_{1-42}$ or $A\beta_{1-40}$ mediated gold colloid aggregates. It was concluded that a β -sheet conformation identified in previously reported in AD mouse/human brain tissues was in volved in a formation of the gold colloid aggregates.

1. Introduction

Amyloidogenic or amyloid beta $(A\beta)$ peptides, such as $A\beta_{1-40}$ or $A\beta_{1-42}$ are regarded as hallmark neuropathological biomarkers associated with the neurobiological mechanisms contributing to and observed in clinical populations afflicted by Alzheimer's disease (AD) (Moser et al., 1995; Pujol-Pina et al., 2015; El-Shimy et al., 2015; Attanasio

et al., 2013). The process in both observation and characterization of the terminal amyloid fibrils have been extensively investigated (Smith et al., 2006; Zurdo et al., 2001; Langkildea and Vestergaard, 2009; Colvin et al., 2015). Notably, amyloid fibrils are usually several hundred micrometers (µm) in size and consist of pre-fibrils, which are comprised of unit oligomers (Bhatia and Deep, 2013; Chung et al., 2001; Giovanna et al., 2010; Frydman-Marom et al., 2011). Thus, the formation and

E-mail address: yokoyama@geneseo.edu (K. Yokoyama).

^{*} Corresponding author.

establishment of pre-fibrils (i.e., fibrillogenesis) may provide unique insight and opportunity for interventions if the neurobiological mechanisms underlying such processes can be elucidated and manipulated to forestall AD neuropathological biomarkers. Therefore, the formation of unit oligomers from soluble and nontoxic monomers is regarded as the key intermediate in the process of fibrillogenesis and is considered to be a reversible process (i.e., at least in part in the earlier stages of pathogenesis) that may provide a therapeutic opportunities for treating both early and more progressive stages of AD. Alternatively, the formation of fibrils or pre-fibrils is considered an irreversible processes in later stages of AD; hence, it becomes a progressive neurodegenerative process once these pathological (pre-)fibrils form and alter the neural circuitry they govern. The mechanism(s) underlying the formation of the nuclei-based pre-fibril is/are considered to be the most reasonable method(s) for interpreting the fibril formation and the most logical treatment process (Yokoyama et al., 2019). A key stage in this fibrillogenesis is the formation of an intermediate oligomer through a reversible process, which then leads to the formation of one-directional pre-fibrils (Makin and Serpell, 2004). A major conformational change of the monomer to an intermediate oligomer requires significant protein folding, and further requires a Gibbs energy of -10 kcal/mol (Heinz et al., 2009, 2008; Venditti et al., 2015) based on computational calculations. The most important on-set process of any fibrillogenesis is the interactions and protein-to-protein networking between these peptides (i.e., to better understand the physical chemistry of these protein interactions); especially, prior to initiating a neuropathological processes. Considering that more progressive fibrils are formed irreversibly, the networking between peptides must be "effective" and occur due to strong interactions; thereby, suggesting that there ought to be a positive linear relationship between these peptides and fibrillogenesis interactions that could be observed. However, a direct investigation of this networking process is still lacking and any confirmation of such peptide and fibrillogenesis interactions remain to be elucidated.

Under in-vitro conditions, the self-assembly of gold colloid aggregates coated with amyloidogenic peptides was previously investigated (Yokoyama et al., 2019; Yokoyama, 2010, 2011a, 2012; Yokoyama et al., 2015) and these studies revealed that the peptides were relatively small, amphiphilic peptides (i.e., consisting of both hydrophilic and hydrophobic segments) and the temperature/pH conditions for folded/unfolded conformations warranted further study. The advantage of this system was that it utilized a monomer peptide that can be prepared on the nano-surface by orienting each peptide so that it may undergo the most effective networking process (i.e., optimizing putative interactive protein-to-protein physicochemical processes, that in turn, may make it both more sensitive and probable to investigate such peptide events at the preclinical level). Peptides are adsorbed over the nano-surface and are used to make physicochemical connections between two adjacent nano-particle surfaces by making simulated and contrived networks between peptides. Because of the networking properties between such peptides, the physicochemical assembly to the gold colloidal forms aggregates, that in turn, results in a drastic change in its spectroscopic features (i.e., the networking process itself can be spectroscopically probed). Therefore, the investigation of the formation of aggregates (i.e., whether simulated, contrived, or pathological in nature) might be uniquely preclinically explored through this method to provide critical information on how nanoscale surface potentials may physically interact with the chemistry of a peptide and whether a specific structure can be selectively constructed (Yokoyama, 2010, 2012). Also, the adsorption of proteins over the nano-particles has been extensively investigated as a protein corona (i.e., modifying or modulating the nano-particles characteristics, hydrodynamics diameter, and surface charges), and drawing a great interest and attention in terms of designing new bio-nano-materials with the potential for therapeutic interventions (Hooshmand et al., 2021; Rahman et al., 2013; Lundqvist et al., 2004; Wolfram et al., 2014; Huang et al., 2021; Latreille et al., 2022). Many important applications of controlling the immune response (Neagu

et al., 2017; Sahneh et al., 2013; Boraschi et al., 2017; Farrera and Fadeel, 2015; Corbo et al., 2016) or vulnerability to toxicity, *in-vivo* clearance, cellular (re)uptake, and signal transduction (Salvati et al., 2013; Nejadnik et al., 2018; Konduru et al., 2017) have been directed towards approaches that could utilize the protein corona. The aggregation process through the protein corona reveals a broad array of formation mechanisms and roles for protein-to-protein interactions (Zhdanov and Kasemo, 1998; Galdino et al., 2021).

It was hypothesized that the peptide-to-peptide physicochemical networking must be established by an unfolded conformation of each peptide, and this unfolded conformation in tune, would be strongly enhanced at the nano-particle surface. As observed in negatively charged micelles and Teflon particles, the β -sheet formations of A β on hydrophobic graphite surfaces (Kowalewski and Holtzman, 1999) or at air-water interfaces (Schladitz et al., 1999) indicate an involvement of interfacial surface potentials that are methodologically utilized for the purpose of conforming an intermediate oligomer (Kusumoto et al., 1998; Coles et al., 1998; Shao et al., 1999; Giacomelli and Norde, 2005; Rocha et al., 2005). The functionalities of peptide coated nano-materials have remarkably broad applications in areas where the nano-size can have significant effects, (Norde, 2008) including nano light switching devices, (Cook et al., 2012) disease controlling materials combined with DNA, (Muangchuen et al., 2014) DNA biosensors, (Rasheed and Sandhyarani, 2014) control of human cellular activity, (Suarasan et al., 2015) photo-dynamic therapy, (Zhao et al., 2014) and optical biosensors that quantify heavy metal pollution in water (Politi et al., 2015). However, very little is known regarding how the aforementioned proteins adhere to nanoscale solid surfaces which is required to increase our understanding of these broad ranging applications and to develop new methodologies for addressing these unresolved issues.

The goal of the present study was to test if the preclinical AD rodents models possesses the amyloids which impact and cause externally inserted gold colloids to form the gold colloid aggregates. Thus, the gold colloid aggregates would then enable identification of amyloid fibril locations within the brain (*i.e.*, a crucial spot detection procedure) or the more detailed conformations or network for forming the amyloids crucial to result in AD.

The present study employed the Long Evan's Cohen's AD rat model to examine the hippocampus to target the fibrils and investigate its ability to interact with gold nano-particles. If any active peptides were present in the AD rat hippocampus, then it may adsorb over the nanogold colloid's surface. An *in-vitro* study using $A\beta_{1-40}$ or $A\beta_{1-42}$ monomer coated gold colloid formed clear aggregates only when under the acidic condition (*i.e.*, pH ~4) (Yokoyama et al., 2009). Thus, in principle, no gold colloid aggregates should be formed under pH conditions of the AD rat brain (*i.e.*, pH 7.0–7.4). Any detection of gold colloid aggregates would strongly suggest the existence of oligomer-like $A\beta$ induced peptide-peptide interaction and it simultaneously supports that the conformation created at acidic conditions *in-vitro* contains in oligomer-like conformation over nano-gold surfaces.

This work utilized Surface Enhanced Raman Scattering (SERS) imaging to detect and seek out the compounds of interest mediating the gold colloid aggregates. Under *in-vitro* conditions, the gold colloid aggregates were formed through peptide-peptide interaction of unfolded A β_{1-40} monomers or possibly oligomers conformation at an acidic (pH \sim 4) condition over nano-gold surfaces. Therefore, the focus of this study was to confirm if any sign of gold colloid aggregates was possible in the AD rat brain (*i.e.*, in which the pH 7.0–7.4 is far from pH \sim 4). If this is the case, then it would permit an opportunity to attempt to identify the mediates supporting the gold aggregates. However, the formation of aggregates due to the external deposition of gold colloid to AD rat brain has never been investigated; thus, making this study with the SERS methodology for AD preclinical research.

The challenge of this work was to characterize the signal levels by which optimal fibrils and gold colloid aggregates could be reliably detected. It is important to note that no significant amount of the SERS

would occur if the gold colloids failed to form the aggregates; thereby, offering a rather sensitive and precise measurement methodology for the present preclinical study. This preliminary report attempts to establish an approach for using a Raman detection scheme of amyloid fibrils adsorbed over the gold nano-colloids for the methodological assessment of AD pathology in preclinical rodent models. While this study adopted SERS imaging as an imaging method, a counterpart imaging methodology utilized surface plasmon in Raman signal detection is TERS (Tip-Enhanced Raman Scattering), which can provide angstrom-scale spatial resolution. However, considering the issues involving probe contaminations and relatively short lifetime of scanning probes prevents the consistent and steady data. Furthermore, the sensitivity of signal is known to be very low and it makes interpretation of TERS spectra non-straightforward and angstrom-scale spatial resolution could not be consistently obtained (Rizevsky and Kurouski, 2022).

2. Materials and methods

All procedures and ethics approval were obtained by the SUNY Old Westbury Institutional Animal Care and Use Committee (Protocol # 1706001). Note: There were no commercial restrictions from either vendor for such cross-breeding. The AD transgenic rat model was obtained by cross-breeding commercially available #699 F344-Tg(Prp-APP, Prp-PS1)19/Rrrc female rats from the Rat Resource & Research Center (Rrrc: Columbia, MO) with a standard outbred Long Evans (LONGEV-M) male rats (Taconic: Germantown, NY) to produce a heterozygous Long Evans Cohen's AD transgenic rat model. From these offspring, the Xlinked Cohen's AD transgenic rats were passed onto the F1 generation offspring and only Long Evans rats were selected for and then continuously in-bred in each subsequent generation to obtain a homozygous Long Evans AD rat. This process was repeated for at least three generations. The rat's tails were clipped at the tip and again following sacrifice to be used for genotyping to determine heterozygous vs. homozygous for the targeted conservation of the AD trait. The rat tails were subjected to qRT-PCR using 10 mM primers of APP and PS1 to detect its expression (Jankowsky et al., 2005) using a commercial EZ Tissue/Tail PCR genotyping kit (G1001-100; EZ BioResearch, LLC: St. Louis, MO) and the product ran on a 0.8% agarose gel followed by the bands imaged on a UV Transilluminator. The PCR primers were as follows: (R699 mPrp Forward 5'-3') CCTCTTGTGACTATGTGGACTGATGT; (R699 mPrp Reverse 3'-5') GTGGATACCCCCTCCCCAGCCTAGA; (R699 PS1 Forward 5'-3') CAGGTGGTGGAGCAAGATG. The F1 generation were genotyped and only Long Evans Hooded rats with the AD transgenic traits were rebred.

Next, the F2 generation were then used to establish a breeding colony of the Long Evans Cohen's AD rat model (*i.e.*, the first established modified Cohen's AD model using pigmented rats that have a greater range of cognitive ability given their increased visual acuity over non-pigmented rats).

The rats were then aged to postnatal day 55 (i.e., following maturation of the prefrontal cortex), then deeply anesthetized with isoflurane. Once non-reflexive, the rats were euthanized, and their brains extracted in under 2-min. Subsequently, their hippocampi were then sub-dissected and into ${\sim}500~\mu m$ sections separating out the anterior, middle medial, and posterior portions with 2 sections of each, stored in 1.5 mL Eppendorf tubes and stored at $-80\,^{\circ}\text{C}$ before being processed for Raman detection. As shown in Fig. 1, the middle section of the hippocampus was then defrosted and mixed with gold nano-particles. Gold nano-particles were purchased from Ted Pella, Inc. (Redding, California, USA) and have the following estimated diameters (d), $d = 80 \otimes 1.0 \text{ nm}$). The gold nano-particles 800 μL was mixed with the tissue for ${\sim}12\,h$ under 4 °C. Then, the tissue was soaked in distilled and deionized water for an hour in order to rinse off the gold nano-particles, which were plausibly physisorbed over the tissue surface. Then, this tissue sample was placed over the mica disks, and subsequently placed in a closed case being purged with nitrogen gas (99.99%) overnight (~ 24 hrs) to conform a dried status.

Lyophilized powder of A β_1 $_{-40}$ peptide (MW; 4.3 kDa, 97% Mass Spec. purity) and A β_1 $_{-42}$ peptides (MW; 4.5 kDa, 97% Mass Spec. purity) were purchased from r-Peptide (Bogart, GA, USA). Aqueous 220 μ M stock solution of A β_1 $_{-40}$ and A β_1 $_{-42}$ were stored at -80 °C. The optimized ratio between all peptides and gold nanoparticles was set as 1000:1 so that the concentration of gold nanoparticles was roughly 300 pM. Attachment of the peptides to the gold colloidal surface was known to be achieved almost instantaneously and considered to reach equilibrium within a minute. The pH of the solution was achieved by adding either HCl or NaOH to the solution. The volume of 50 μ L of solution was dropped over the Atomic Force Microscope (AFM) mica disc of grade V1 mica, 0.21 mm thick 10 mm diameter purchased from Ted Pella, Inc. (Redding, California, USA) and it was air-dried overnight.

Next, the Raman spectra were collected by using a WITec Raman alpha300R (WITec, GmbH, Ulm Germany) confocal Raman imaging system. The microscope can be used for automatic scanning of the specimen using a computer-controlled sample stage. A laser with wavelength of $\lambda=633$ nm at 0.5 mW power was used for excitation through a $100\times$ objective (Zeiss, 0.9 NA). Here, spatial resolution was calculated by $0.61\times \lambda/NA\sim0.43$ µm. The Raman-scattered photons

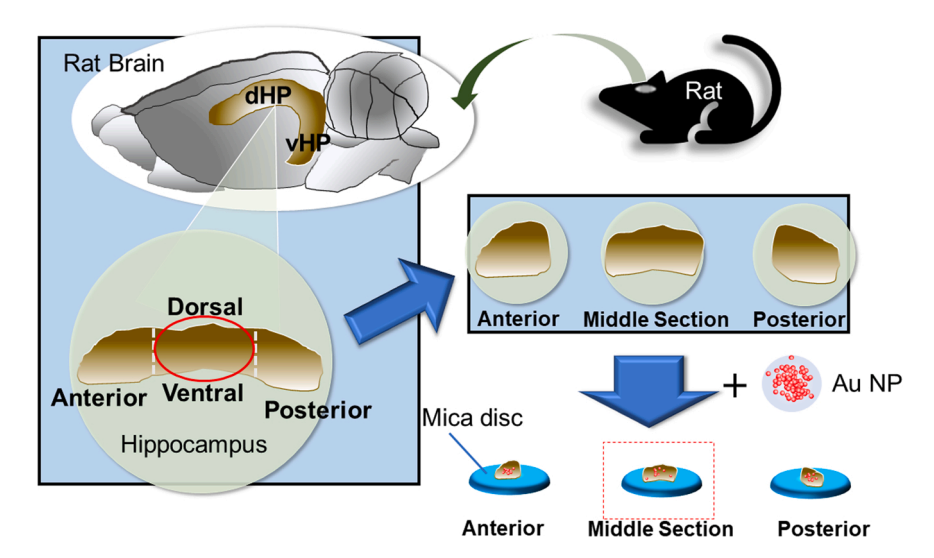


Fig. 1. The sketch of the AD rat brain and hippocampal inset illustrating the sub-dissected tissue samples. The portion of the AD rat hippocampal brain sample tissue studied in this work is marked by the red oval. The gold nano-particles were mixed with the tissue. Then, this tissue sample was placed over the mica disks.

were collected through a photonic fiber and directed to a 300 mm spectrograph equipped with a 600 gr/mm grating and thermoelectric cooled CCD detector. To conduct the experiments, a grid consisting of 100×100 pixels and covering an area of $20~\mu m\times20~\mu m$ was selected over the white-light image and 10,000 spectra/maps with an integration time of 500 ms/spectrum and a lateral spatial resolution of 0.43 μm were acquired. The Raman spectrum in the region of $\sim\!300$ to $\sim\!3900~cm^{-1}$ was collected.

The collected data of the Raman image and the associated Raman shift information were processed with Project Five 5.3 (WITec, GmbH, Ulm Germany). For the case of extracting the band components of each sample spectrum, it was processed with a component of the band expressed by a Gaussian profile by Peak Fit function of OriginPro 2018b (OriginLab Corporation, Northampton, MA USA), and the spectrum area, weight, and average peak position of the spectrum in the targeted region (Yokoyama, 2011a).

3. Results

The white-light images of a part of the AD rat hippocampal brain tissue sample is shown in Fig. 2(a) in \sim 1 mm $\times \sim$ 0.7 mm region and Fig. 2(b) magnified to \sim 200 µm $\times \sim$ 150 µm region. In Fig. 2(b), the substance shown at the central spot within a red box section was identified as gold colloid aggregate. The further blown-up image of the squared area is shown in Fig. 2(c). There were identifiable amyloid fiberlike shadows spotted around the gold nano-particle aggregates, and those shadows of interest were indicated by the dotted line as a guide in Fig. S1. The region marked with a red square in Fig. 2(c) (or Fig. 3(a)) was scanned for constructing the Raman imaging shown in Fig. 3(b). The two major Raman spectral features A and B were found as shown in Fig. 3(c) with a substrate or background component C. The color map shown in Fig. 3(b) associated the color given in Fig. 3(c). (component A: red, component B: green, component C, blue). The yellowish colored region, therefore, is considered to be a combination of component A (red) and component B (green). Among all data observed from within the Raman spectrum, a representative and well-resolved spectrum was detected at the spot marked with "+" in Fig. 3(a) and is shown in Fig. 4. The region contains spectral features of components A or B significantly coincide with the location identified as fiber-like shadows were existent (See Fig. S2). While the spectral features observed in Component B weren't well resolved, further analysis of spectral components was attempted. Here, the region of 400–3000 cm⁻¹ in component B was fitted with the Gaussian profiles and four components were extracted (See Fig. S3 and Table S1 (a)) peaks responsible for the region ≥ 1900 cm⁻¹ were summarized in Table S1 (b) supporting that main features observed in component B in Fig. 3(c) matched with those Raman shifts reported for AD mouse or human patients tissue (Guo et al., 2019; Szekeres and Kneipp, 2019; Yu et al., 2018; Walther et al., 2002; Stewart and Fredericks, 1999; Dong et al., 2003; Carey, 1982; Harada and Takeuchi, 1986; Overman and Thomas, 1999; Yokoyama et al., 2022). In order to conduct a further detailed investigation of how aggregates were formed, the most well-resolved Raman shift spectrum in

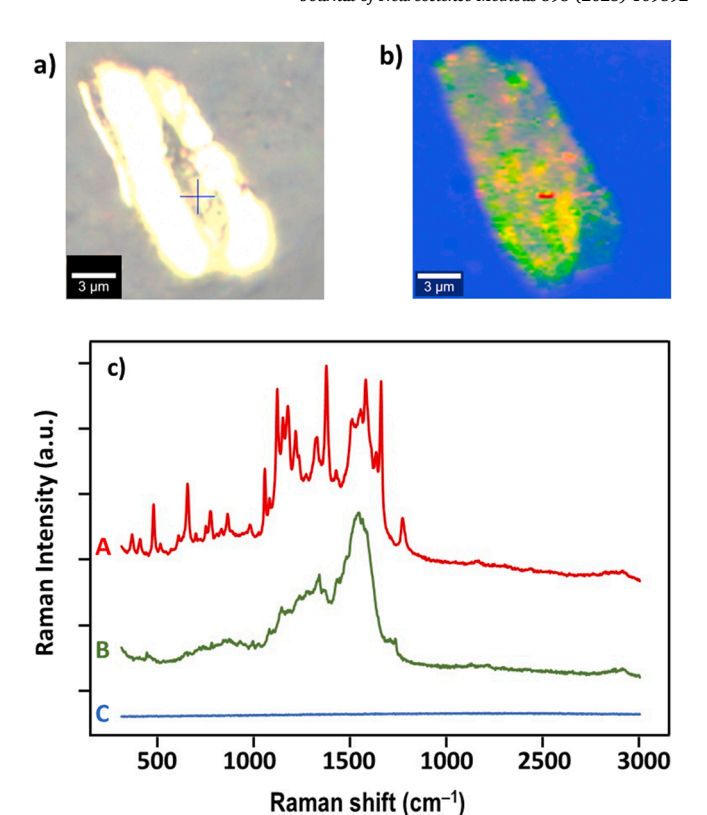
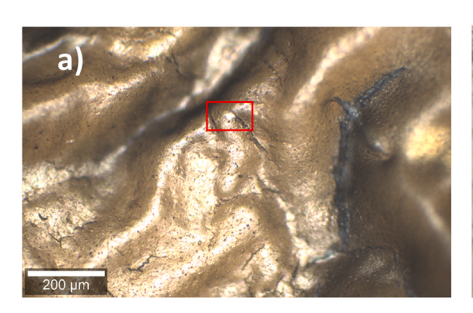
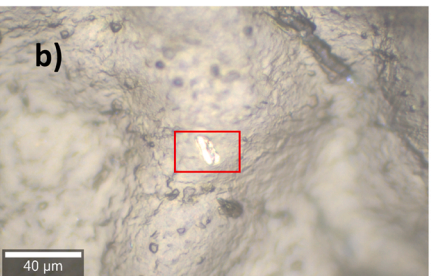


Fig. 3. a) The white-light image of a section of the tissue marked by a red square box in Fig. 3 c) with \times 100 magnification. In here, the location marked by "+" was chosen to collect the Raman spectrum shown in Fig. 4. b) The Raman imaging map of gold colloid aggregates shown in a). c) The Raman shift spectrum of the components A and B and base line (Component C). The color of each component corresponds to those shown in Raman image in b).

component A shown in Fig. 4 was analyzed in two schemes. First, the major peak lines were assigned based on the reported Raman shift (or IR vibrational frequencies) (Guo et al., 2019; Szekeres and Kneipp, 2019; Yu et al., 2018; Walther et al., 2002; Stewart and Fredericks, 1999; Dong et al., 2003; Carey, 1982; Harada and Takeuchi, 1986; Overman and Thomas, 1999) as summarized in Table 1 (and Table S2) for more details. The observed modes were also examined and were approached to be assigned with the Raman shift wave numbers observed in AD mouse brain, (El Khoury et al., 2021; Ji et al., 2018; Mattana et al., ; Palombo et al., 2018) AD human brain, (Dong et al., 2003; El Khoury et al., 2021; Lochocki et al., 2021) as well as mouse retina tissue, (Stiebing et al., 2020) and they were subsequently matched with the closest Raman shift peaks (See Table 1 (and Table S2), right half columns). In order to investigate and compare the gold colloid aggregates being formed in-vitro, the SERS spectrum was collected for the in-vitro condition in $A\beta_{1-40}$ or $A\beta_{1-42}$ coated in 80 nm gold colloid under pH ~4, pH ~7, and





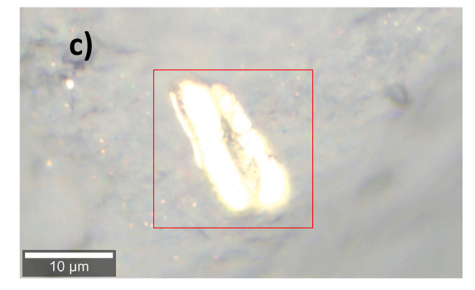


Fig. 2. a) The white-light image of a section of the tissue with \times 10 magnification. b) The white-light image of a section of the tissue marked by a box in a) with \times 50 magnification. c) The blow up of the region marked with red box in b) with \times 100 magnification.

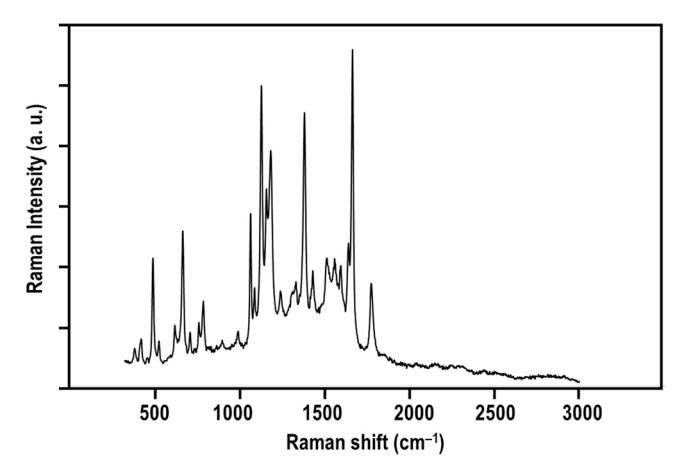


Fig. 4. A representative SERS spectrum collected at the position marked by "+" in Fig. 3a). The mode assignments are given in Table 1 and Table S1.

Table 1

The major Raman spectral lines (\widetilde{v}_{obs}) picked from Fig. 4 and shown in Fig. 7(a) with assignments (Jankowsky et al., 2005; Guo et al., 2019; Szekeres and Kneipp, 2019; Yu et al., 2018; Walther et al., 2002; Stewart and Fredericks, 1999; Dong et al., 2003; Carey, 1982; Harada and Takeuchi, 1986).

$\widetilde{\nu}_{obs}$ (cm ⁻¹)	Assignment
419	Trp
455	C-S stretching
487	S-S stretching
522	N-H deformation, S-S stretching, skeletal, deformation
617	Tyr C-S stretching, COO- wag of backbone, COO- wag (Leu-Gly-Gly),
	COO ⁻ wag (Ala-Pro-Gly)
663	Tyr C-S stretching
707	C-S stretching, COO ⁻ deformation, Met sulfoxide
757	Indole symmetric breathing mode, Trp
864	C-C stretching (Phe-Gly-Gly-Phe), C-C stretching (Gly-Gly-Phe), C-C
	stretching (Phe-Gly-Phe-Gly)
898	C-C stretching (Gln), C-C stretching (Ala-Ala)
988	C-C stretching, β-sheet or Phe
	*C-C stretching C ₂ -t ₂ t ₂ mode (Grys et al., 2020)
1061	C-N stretching
1085	C-C stretching, C-N stretching (Ala-Ala-Ala), C-N stretching (Leu-Gly),
	Lys, Arg, Gln, Asn
	*C-C stretching bi-dendate binding-adatom induced C ₂ t ₂ mode (Grys
	et al., 2020)
1125	Val, Ile, C-Cα and C-N stretching, NH ₃ deformation (Leu-Gly-Gly)
1156	C-N stretching, Phe-Gly-Gly-Phe,
1180	Tyr (IgG)
1240	CH ₂ wag (Leu -Gly), Amide III in β-sheet
1313	CH ₂ wag (Gly-Leu), CH ₂ wag (Gly-Gly-Phe), CH ₂ wag (Phe-Gly-Phe-Gly)
1329	CH ₂ wag (Leu-Gly), CH ₂ wag (Gly-Gly-Phe), CH ₂ wag (Phe-Gly-Gly-
1000	Phe), Trp and Tyr (IgG)
1379	CH ₂ scissors, CH ₃ symmetric bend (Ala-Ala), *symmetric stretching
1.400	COO ⁻ -Au
1430	CH ₂ scissoring motion (Lysozyme), CH ₂ scissoring motion (Glu), CH ₂
1511	deformation,
1511 1559	Phe, His, Trp (Lysozyme) Trp, Trp + His (Lysozyme), Trp (IgG), benzene ring stretching, pyrrole
1339	ring stretching,
1592	deformation benzene ring, benzene ring stretching, Amide II Phe Tyr
1392	(protein), Guanine Adenine (DNA/RNA), Phe, COO ⁻ asymmetric
	stretching, OH mode, Ring CC stretching, *Citrate ν_a (COO ⁻) (Grys et al.,
	2020)
1640	Amide I in lysozyme, Amide I in Phe-Gly-Gly-Phe
1661	C=O stretching, Glu, Amide I in insulin, Amide I in Ala-Pro-Gly, Amide I
	in β-sheet
	1

pH \sim 10. Among the collected spectra, the focus was on the hybrid of the two spectra (Type I in Fig. 5 and Type II in Fig. 6) from those A β_{1-42} coated in 80 nm gold colloid under pH \sim 4 that could explain what was observed in the AD rat hippocampal brain tissues (Fig. 4). The white-light image of two types and distribution map of each spectral

components are also shown in Fig. 5 and Fig. 6. It clearly shows that those shown in Fig. 5(a) and Fig. 6(a) exhibit significantly different morphology from that of AD rat brain hippocampal tissues shown in Fig. 3(a). The summary of comparison and indication of the matching of the spectrum features are shown in Fig. 7 and summarized in Table S2. The observed modes (Fig. 4 and Fig. 7(a)) were compared with those observed in Raman signals of gold colloid aggregates of A β_{1-42} coated 80 nm gold. (Fig. 7(b) - Type I and Fig. 7(c) - Type II) The morphology of gold colloid aggregates were also examined between these two different systems (See the inserts of Fig. 5).

4. Discussion

This unique and pioneering study showed that a relatively simple treatment of and AD-positive rodent preclinical brain tissue with gold nano-particles prepared gold aggregates of the area size of ~100 μm² could be used as an approach for detecting possibly amyloid fibrils for investigating the mechanism of the fibrillogenesis of AD at the preclinical level, while a significant amount of gold nano-colloid particles (not aggregates) were detected, they did not possess detectable Raman signals indicating no peptides were coated to provide SERS signals. There was a sign of spatial overlap between the gold colloid aggregates located near or surrounded by areas where the amyloid fiber-like shadows were present (See Fig. S1). Since the white light image failed to distinguish the spatial overlap apart from the shiny appearance of the tissue or gold particle aggregates, the final confirmation as gold aggregates was made by detecting the Raman signal as shown in Fig. 3 (c). The surface of the tissue remained as it was dried, so that it was not completely flat. It was typically noticed at \pm 20 μm of the vertical surface height differences within a surface of one gold colloid aggregate. The feature in component B in Fig. 3(c) was also understood as detecting the ensembles of the different degrees of interaction between peptides or peptide and gold particle surfaces within 300 nm \times 300 nm range.

The study on the process of amyloidogenic peptides coated gold colloids aggregations, (Yokoyama et al., 2019; Yokoyama, 2012; Yokoyama et al., 2009; Yokoyama, 2011b, 2013; Yokoyama et al., 2008, 2010; Yokoyama and Welchons, 2007) was concluded to be highly enhanced at an acidic condition (i.e., pH $< \sim 4.0$). However, cluster-like particle ensembles of bare gold colloid was observed at pH $<\sim 3.0$ (Yokoyama et al., 2009; Yokoyama et al.,). The most plausible reason for bare gold aggregation was considered by mediation of citrate, which is often used to stabilize the gold colloidal surface. The reported contents of citrates of gold colloids used in the present study is at negligible levels, whereby possessing traces of citrate is $< 10^{-5}\%$ (Yokoyama, 2010). In the employed mode assignments, there were only three modes (1085, 1379, and 1592 cm⁻¹) matched with those reported for citrate mediating gold colloids and leading gold colloid aggregates (See Table S2) (Grys et al., 2020). Therefore, speculated that the affinity of the detected component to the gold surface exceeds that of citrate to the gold surface resulting in the replacement of citrate. To support this idea, there is a report of a significant interaction between gold surfaces and amino acids suggesting hydrogen bonding between a hydroxyl group and gold (OH-Au) (Rai et al., 2012; Torsten et al., 2018). Through the simulation of examining the adsorption orientation, it was concluded that the hydrophobic segment of peptide was interacting with the gold surface through electrostatic forces (Yokoyama et al., 2019).

The aggregation morphology was clearly different between aggregates observed in mice brain tissues (Fig. 2(c)) and the aggregates of $A\beta_{1-42}$ coated 80 nm gold colloids formed at pH < 4 (Fig. 5(a) and Fig. 6 (a)) (Yokoyama et al.,). The remarkable feature in shape difference was that the $A\beta_{1-42}$ coated gold colloid aggregates possessed round edge and forming various patterns of aggregates forms. Alternatively, the observed gold aggregates in the rat brain possessed bulky solid-like appearances where the edges were almost smooth. A clear difference was also found in physical size, where the aggregate size of $A\beta_{1-42}$ coated gold colloid varied in their sizes ranging between few μ m² and

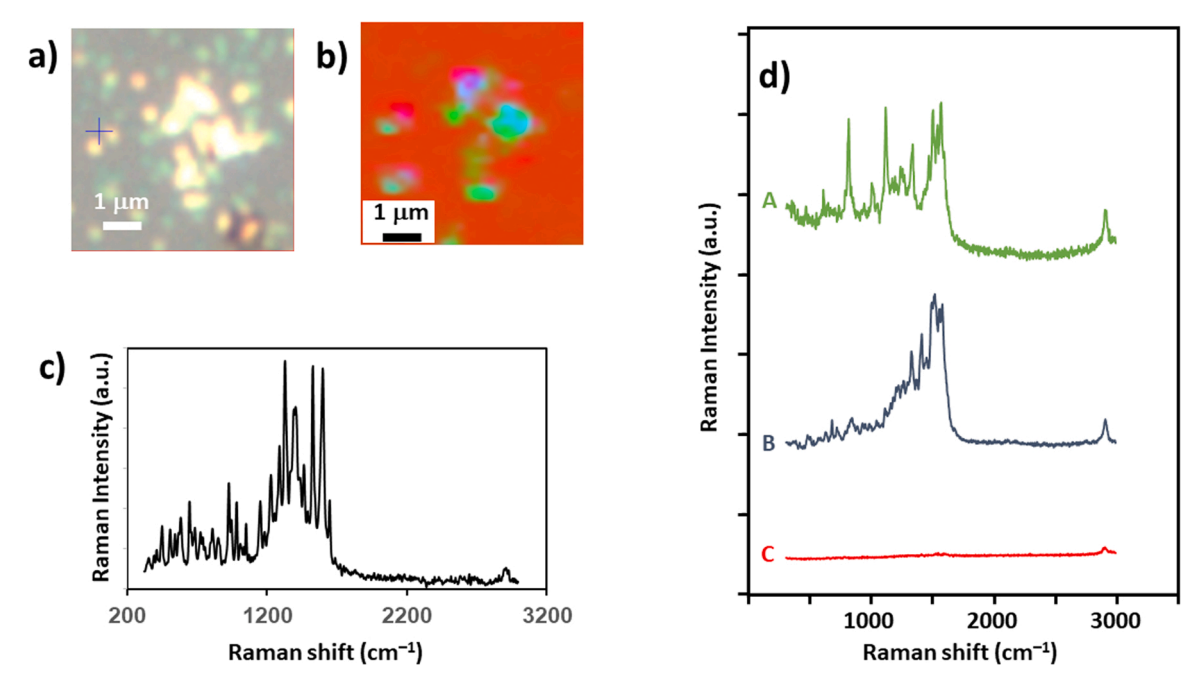


Fig. 5. a) The white-light image with \times 100 magnification of A β_{1-42} coated 80 nm gold particles under pH \sim 4. b) The Raman imaging map of gold colloid aggregates shown in a). c) The representative SERS spectrums (Type I) sampled at + position in a). d) The Raman shift spectrum of the components A \sim C. The color of each component corresponds to those shown in Raman image in b).

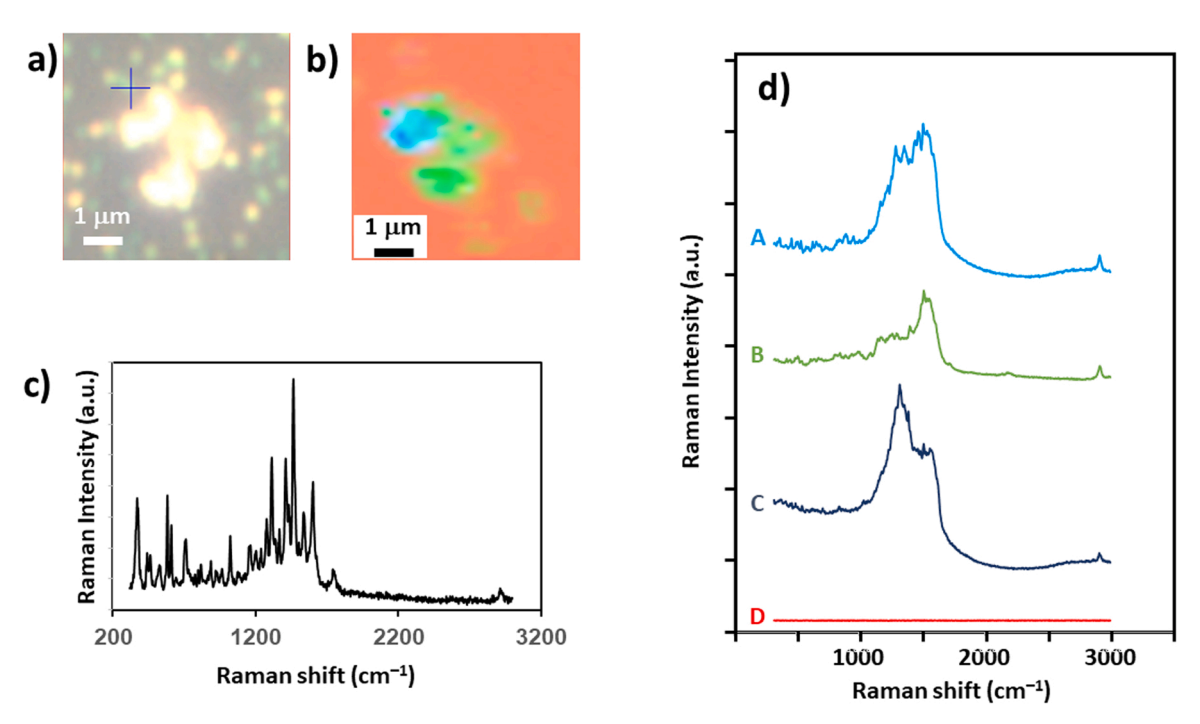


Fig. 6. a) The white-light image with \times 100 magnification of A β_{1-42} coated 80 nm gold particles under pH \sim 4. b) The Raman imaging map of gold colloid aggregates shown in a). c) The representative SERS spectrums (Type II) sampled at + position in a). d) The Raman shift spectrum of the components A \sim D. The color of each component corresponds to those shown in Raman image in b).

tens of μm^2 . The gold colloids aggregates formed in the diseased rat brain tissue possessed the area of $\sim 80-100~\mu m^2$.

The spectral component of Raman imaging observed in Fig. 3(b), 5 (b), and 6 (b), contained relatively similar features as seen in component B in Fig. 3(c), component B in Fig. 5(d) and Component B in Fig. 6(d) which can be explained by being conformed by CH₂ wag of Amide III band in β -sheet ($\sim\!1263~\rm cm^{-1})$ and benzene ring (or pyrrole ring) stretching (see Table S1). The most detailed SERS spectral features of the AD positive rat shown in Fig. 4 (and listed at Table 1) possessed a

significant amount of matching with those observed in AD mouse or AD human tissue (Table S2). Except for two modes (*i.e.*, $378 \, \mathrm{cm}^{-1}$ and $1772 \, \mathrm{cm}^{-1}$), all modes were assigned from the Raman or IR spectral features of amino acids from the previous studies (Guo et al., 2019; Szekeres and Kneipp, 2019; Yu et al., 2018; Walther et al., 2002; Stewart and Fredericks, 1999; Dong et al., 2003; Carey, 1982; Harada and Takeuchi, 1986; Overman and Thomas, 1999). The modes considered to be highly associated with β -sheet at 1240 cm⁻¹ and 1661 cm⁻¹ were observed and supporting the presence of β -sheet as a main and critical

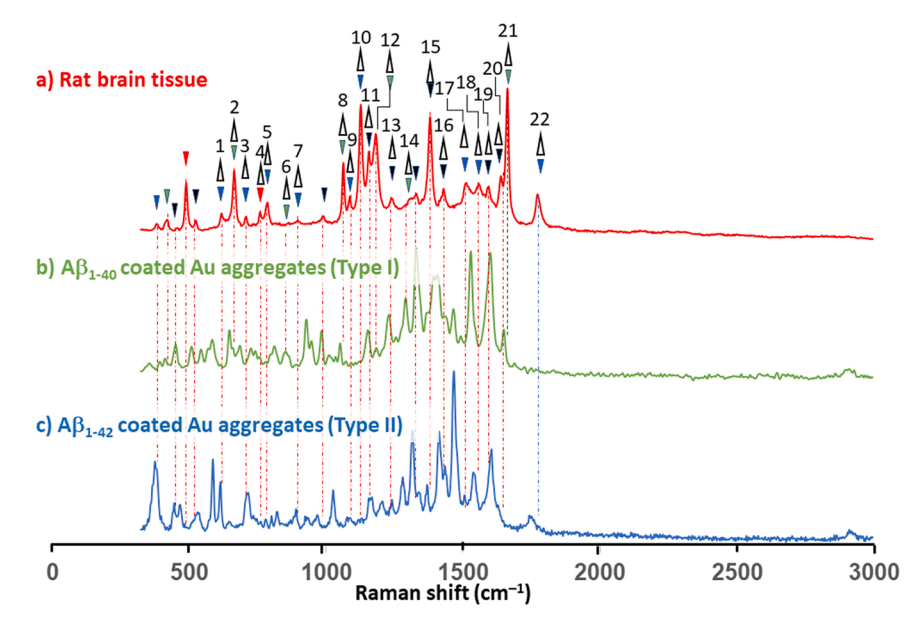


Fig. 7. The comparison of the Raman spectrum, and here the y-axis is in an arbitrary unit by locating each spectrum normalizing the highest count to the same for each in order to clarify the shift position. a) representative SERS spectrum detected at a tissue sample and an identical one shown in Fig. 4. b) and (c) two representative SERS spectrums of $A\beta_{1-42}$ coated 80 nm gold particles under pH~4 shown in Fig. 5 c) and Fig. 6 c). In order to correspond the observed peaks in a) to b) and c), the line positions were guided and indicated the matching. If the line position of spectrum a) matches with that of (b), (c), or with both (b) and (c), the green, blue, or black reverse triangle was shown on the top-of-the-line position, respectively. If there was no matching red reverse triangle was shown. The bands correspond to those observed in Alzheimer's disease patient tissue (Lochocki et al., 2021) were listed with open triangles with number corresponding to those listed in Table S2.

conformation of the amyloid fibril-like structures. Since these modes were found in the Raman spectrum of Aβ₁₋₄₂ coated gold colloid aggregates, it was therefore logically deduced that the β-sheet formation must be a major component to form gold colloid aggregates through this approach. Although no exact matching in Raman shift did not occur, the spectral features in the AD rat brain hippocampal tissue was explained by two spectral features combined Type I and Type II. There were 19 modes which were identified in the AD positive rat brain hippocampal tissues that were consistent with those observed in AD rat or AD human tissues as marked with open triangle and number listed in Fig. 7(a) and Table S2. Among 29 observed Raman spectral lines (listed in Table S3 on the left), 17 lines were reported in the studies of AD mouse/human tissue (Guo et al., 2019; Szekeres and Kneipp, 2019; Yu et al., 2018; Walther et al., 2002; Stewart and Fredericks, 1999; Dong et al., 2003; Carey, 1982; Harada and Takeuchi, 1986; Overman and Thomas, 1999; El Khoury et al., 2021; Lochocki et al., 2021) (El Khoury et al., 2021; Ji et al., 2018; Mattana et al., ; Palombo et al., 2018; Stiebing et al., 2020) (El Khoury et al., 2021; Stiebing et al., 2020) justifying the high involvement of β -sheet formation (e.g., $\Delta 13$, $\Delta 15$, and $\Delta 21$). The modes assigned to be associated with Trp and Pro suggest the possibility of other substances present in a tissue, since these amino acids are not the components of $A\beta_{1-42}$. The non-exact matching in wave numbers can be explained as an effect of conforming gold aggregates.

Since the prominent modes observed in spectrum a) in Fig. 4 or Fig. 7 (a) (487, 663, 1061, 1180, 1125, 1379, and 1661 cm⁻¹) were not the same as those found with relatively high intensities in spectrum Type I in Fig. 5(c) or Fig. 7(b) (1328, 1527, and 1649 cm⁻¹) or in spectrum Type II in Fig. 6(c) or Fig. 7(c) (376, 585, 1314, 1411, 1466, and 1602 cm⁻¹) the protein conformation created to support gold aggregates *in-vitro* could not be fully justified as an identical to those found in the AD rat brain hippocampal tissues. The spectral features observed in the AD rat brain hippocampal tissues can be mainly explained by the combination of two different types (Type I and Type II) of those from *in-vitro* sample with respect to the spectral positions and in spite of discrepancies in spectral intensities.

As a concern of the spectral features in Fig. 4, intensity instability of SERS signal was investigated in detail. If the integration average time was not sufficient, the SERS exhibits inconsistent spectral intensity due to instability of plasmon field. To confirm the consistency of the spectral features in Fig. 4, and it was confirmed that spectral feature was mainly consistent across the spot (see Fig. S4) by taking an origin $(x, y) = (0 \mu m, 0 \mu m)$ at the spot marked as "+" in Fig. 3(a), the spectrum of the Raman

shift were mapped out for the region of roughly ${\sim}10~\mu m~\times {\sim}10~\mu m$ (horizontal: $-5.2 \,\mu m \leq x \leq +5.2 \,\mu m$ and vertical: $-5.2 \,\mu m \leq$ $x < +5.2 \mu m$) along the coordinate indicated in Fig. S4 (a). The featured pattern of the Raman shift distributions were roughly the same for both horizontal (along x-axis) mapping (See Figs. S4(b) and (c) and vertical (along y-axis) mapping (See Fig. S4 (d) and (e)). The flat maps (Figs. S4 (b) and (d)) clearly indicated three belts found in an entire range for both maps. They were found at ~880 cm⁻¹ (corresponding to assignment $\Delta 6$ or $\Delta 7$ in Table S2), ~ 1220 cm⁻¹ (corresponding to assignment Δ 12 or Δ 13 in Table S2), and \sim 1570 cm⁻¹ (corresponding to assignment Δ 18 or Δ 19 in Table 1 and (Table S2)), and these modes were consistent with the analysis made for the component B (See Fig. S1, Fig. S3 (c), and Table S1 (a)). However, the mode at 672 cm⁻¹ observed in component B (Table S1) was too broad to be traced in the map shown in Figs. S4(b) and (d). The mode in around 880 cm⁻¹ is associated with C-C stretching of amino acid frame and that around 1570 cm⁻¹ is associated with stretching of C-C or COO⁻ in benzene or pyrrole ring within amino acid frame. The mode around 1220 cm⁻¹ is considered to be highly associated with β -sheet and implying the high involvement of amyloid fibrils. The range between $\pm\,1.0\,\mu m$ along x- and y-axis was focused, and the spectral features were listed in Figs. S4 (f) and (g). It showed that clear spectral features were observable in a limited area within a rectangular area of $\Delta x = 0.8 \, \mu m$ and $\Delta y = 0.2 \, \mu m$. The choice of axial direction was random, thus it won't conform to a general conclusion though, the horizontal direction maintained the same spectral feature for an entire range where the signals were detected. For a vertical direction, the spectral intensity pattern did not match between the range where the signals were observed, i.e., $(x, y) = (0 \mu m, -0.2 \mu m)$ and $(x, y) = (0 \mu m, -0.2 \mu m)$ $0 \mu m$). Therefore, it can be concluded that spatial resolution of SERS imaging was 0.2 µmin this study.

In this study, another focal point was the detection of the mode strongly interacting with gold colloid surface. While there weren't enough detection hits to study the identifying gold-amino acid interaction to gold colloid aggregates conformed by coated citrates (Grys et al., 2020) reported the band as 1379 cm $^{-1}$ it can be identified as symmetric stretching of COO $^{-}$ -Au, which was not observed in previous studies of AD mouse and AD human brain tissues, respectively. This mode was prominent in the present study's AD rat brain hippocampal tissues and was observed in both patterns of A $\beta_{1\rightarrow 42}$ coated 80 nm gold colloid aggregates as a weak peak. Thus, this mode can be identified as a marker of the present approach using the experimental methodological approach of Raman imaging. Including the mode unassigned at 378 cm $^{-1}$, there

were several modes appear lower than 350 cm⁻¹, (Yokoyama et al.,) and they potentially belong to the modes associated with metal-ligand low frequency modes responsible for Au-amino acid interaction (Ferraro, 1971). As the spectral features were associated with the interaction by the surfaces of the gold nano-particles, the spectral features ranging between 300 cm⁻¹ and 1000 cm⁻¹, maybe associated with the metal-ligand interaction as supported by the report of 348 – 424 cm⁻¹ or $347 - 391 \text{ cm}^{-1}$ for the vibrational mode in gold – phosphorus contained ligand (Ferraro, 1971). Although we still need a further study to confirm, the mode observed in 378 cm⁻¹ in our study (See Table S2) can be associated with metal-ligand mode. In a separate work, the Raman shift in the range of 0-400 cm⁻¹ has been investigated. Some report showed the IR peak around 250 cm⁻¹ was identified as Au-R interaction (R: alkyl group) (Ferraro, 1971) and the peak at $275 \pm 3 \text{ cm}^{-1}$ was observed only when gold colloid aggregates were relatively less-formed (Yokoyama et al.,). This implies only free gold colloid not involved in aggregates exhibit this mode. Thus, as peptide covers over the gold associates for an aggregation the mode at 275 cm⁻¹ may not be responsible for peptide-peptide interaction.

Another mode to note was the one at 1770 cm^{-1} and this mode appeared only in the spectrum of associated with gold colloid aggregates originating from $A\beta_{1-42}$ coated gold colloid under pH 4.0. This mode did not appear in any past reports and the closest mode was 1747 cm^{-1} , which is C=O stretching associated with phospholipids (See Table S2). This assignment was plausible considering it was found in a tissue, making it unlikely to be present in $A\beta_{1-40}$ coated gold colloid system.

The investigation of the distance of the adjacent gold colloid particles, roughly ~2 nm was extracted (Yokoyama et al., 2019). This distance forced to presume the conformation of the peptide to be sheet like conformation, which was also supported by the recent study of TEM on SARS-CoV-2 spike protein conformations over nano-gold surface (Yokoyama). The estimated conformation of each adsorbed $A\beta_{1-42}$ were unfolded conformations leading to maximize the peptide-peptide interaction, while the major conformations of the peptide under pH > 7.0 was considered to be folded conformations or spiking-out orientation. This conformation was considered to be less interactive to conform the aggregates and it was confirmed in the TEM of the $A\beta_{1-40}$ coated gold colloid. The geometrical simulation of the adsorbed peptide exhibited that the spiking out orientation was the best suited conformation (Yokoyama et al., 2019). The spatial overlaps of the location of gold colloid aggregates formation and the presence of the amyloid fiber-like shadows strongly suggest that the gold colloid aggregates were conformed either by β-sheet component of amyloid fibrils or possibly pre-amyloid fibril oligomers (e.g., dimer or trimer) containing β -sheet component.

The observed correlation between the conformation of Ab_{1-40} or Ab₁₋₄₂ responsible for forming gold colloid aggregates and those in the early stage of fibrillogenesis are a primary focus and end goal of this project. The detailed investigation on this line of experimental questioning through the SERS imaging approach is a starting point and remains a promising work in progress. The preliminary results showed that the 80 nm gold aggregates were formed by the interaction of Ab_{1-40} adsorbed over the nano-golds surface, and the change in the feature of SERS spectrum were observed to correspond to the amount of externally inserted Ab_{1-40} , $C(Ab_{1-40})$ (Yokoyama). The more modes grew as C (Ab $_{1-40}$) increases and the intensities of those modes reached to an asymptote showing a completion of the aggregates (i.e., thus, evidencing a positive linear relationship that also saturated). A morphology from the white light image and the degree of densities of the SERS spectral features especially around 400 cm⁻¹ and 1000 cm⁻¹ were definitely observed to be contained within the formation of the gold colloid aggregates that corresponds to the asymptotic stage of the aggregate formations. The spectral features of the asymptote were then subsequently compared with the SERS spectrum shown in Fig. 4 and, interestingly, were found not to have a significant match; thus, implying that this may be due to a rather sensitive difference in detecting aggregates

compositions between the Ab_{1-40} and the Ab_{1-42} amino acid sequences. It was not concluded that the current observation of the SERS spectrum corresponds to the fibril formation and remains to be elucidated. From these findings, the subsequent refined assignments of the SERS spectrum are being characterized as a next step in a future study and it is plausible through this future method to attempt to pin-point the specific amino acid sequences in Ab_{1-40} .

The current spectral features in tissue was best described by the spectral features under pH 4 in-vitro strongly contradicting an instinct of physiological pH condition of the AD rat brain hippocampal tissues. It indicates that the peptide conformation constructed at acidic condition (i.e., ~pH 4) was playing a key role in conforming the gold aggregates. It is still quite plausible, despite the resemblance of modes observed in mouse/human AD brain tissue, the gold colloid aggregates could be constructed without substances associated with amyloids. Within our experimental conditions and time windows, we observed no signs of gold colloid aggregates around the physiologically relevant pH conditions, contrary to a current study which confirmed gold colloid aggregates under physiological pH as shown in Fig. 2(c) or Fig. S7. Thus, the current study suggests that a particular conformation of Ab₁₋₄₂ or Ab₁₋₄₀ is observed to be stable at pH ~4 in-vitro and this situation may be reproduced as a key conformation existent within the transgenic AD rat as a pre-clinical model.

An interaction between the fibrils and the gold colloids are still unknown as to whether the gold colloids are formed with the support of the fibrils warrants further investigation. Based on the theoretical assumption and experimental observations from the present study, the gold surface and Ab₁₋₄₀ or Ab₁₋₄₂ may possess an electrostatic interaction and moreover, the fibrillogenesis can be interrupted as the Ab_{1-40} or Ab_{1-42} adsorb on the gold surface (i.e., as a means to forestall or prevent AD progression in the early stages of disease detection). Alternatively, the fibrils are considered to occur in the terminal stage of fibrillogenesis and no further growths are likely to ensue due to the hydrophobic characteristics being less favorable of the electrostatic interactions with the gold surface. Thus, the formation of the gold colloid aggregates must imply, that at least in part, the oligomeric forms of Ab_{1-40} (or Ab_{1-42}) must serve a role to mediate the electrostatic properties of the gold to adhere to these specific amino acids to form the aggregates being studied. This raises a very interesting point, in which oligomeric formations or monomers are still present even though the rat is transgenic for AD pathology. Considering that the oligomers are generally unstable and may therefore unlikely exist stably in brain tissue samples, the presence of the monomer Ab_{1-40} (or Ab_{1-42}) are entirely plausible. The approach of the present study has to provide a method capable of utilizing Raman detection on the AD positive rat brain hippocampal tissues and identify the component conforming gold colloid aggregates. The most urgent investigation is confirming the presence of aggregates on non-AD rat brain hippocampal tissues. The gold aggregates that were detected in the other two hippocampal brain regions (i.e., the anterior and posterior) are being concurrently analyzed (Yokoyama, et al.,). Those aggregates have a similar dimension as that is observed in this study (i.e., the areas of the aggregate is $\sim 80 \, \mu \text{m}^2$) as shown in Fig. S5. These aggregates were also found in the area surrounded by amyloid fibril-like shadows. The popular diagnosis of the amyloid fibril formation is known to be by ThT fluorescence assay (Malmos et al., 2017). More conclusive results can be confirmed by staining ThT, and the post staining combined with the Raman imaging procedure, which is currently being planned.

Through the Raman imaging technique employed in our *in-vitro* study, the formation of the gold colloid aggregates was possibly considered to be due to the presence of the relatively smaller and soluble units of amyloids or oligomer-like formations inter-connecting with the gold colloids' surfaces. The current method, therefore, can be used as a pre-clinical tool to provide supportive evidence diagnosing AD in transgenic rodents by examining their hippocampal tissue samples treated with gold colloids (*i.e.*, as well as other brain regions). Once the

gold colloid aggregates (as shown in Fig. 2c or Fig. S7) are visually spotted by the white-light images, their SERS signals are further examined to conclude whether the observed spectral features are consistent with those of Ab_{1-42} , which corroborates and supports the tissue samples to be representative of an AD neuropathological biomarker as demonstrated in Fig. 3(b) and Fig. 3(c). Alternatively, instead of examining the hippocampal sample tissues, detection of Ab₁₋₄₂ or Ab₁₋₄₀ in blood samples may also serve as another promising model as an extended application of our current methodology for early detection of AD pathologies. Here, within the blood sample the detection target is the soluble pre-fibrils or oligomers which have yet to reach the insoluble fibrils. From the in-vitro study, it was confirmed that gold colloid aggregates were formed in solution environments with pH or concentrations conditions supporting amyloid aggregation formation. This work showed that only 50 mL of blood sample was needed for a positive detection. After the blood sample was mixed with the gold colloid and left for 12 h at 4 °C, a drop of the mixture was then placed on a plate and dried by nitrogen purge for about six hours to be ready for SERS examination. Then, a visual and spectroscopic inspection searching for gold colloid aggregates was conducted, and the completion of this inspection was done within thirty minutes for a morphological test and about two hours for a detailed SERS signal test.

5. Conclusion

The current study confirmed a formation of gold colloid aggregates with a relatively simpler processing scheme of the AD rat hippocampal brain section with gold-nano particles. As notable remarks, the location of the aggregates was surrounded by the features of amyloid fiber-like shadows implying the high interaction between β -sheet structures and gold colloidal surfaces, thereby resulting in the observed aggregations. The aggregations found in the AD rat hippocampal brain tissues were unique with respect to their physical appearances (i.e., morphology) and their size ranges compared to those observed in *in-vitro* $A\beta_{1-42}$ or $A\beta_{1-40}$ mediated gold colloid aggregates. The spectral features contain β -sheet conformation and those identified in previously reported in AD mouse/ human brain tissues implying the in-situ detection of Raman signal originating from β-sheet formation within gold colloid aggregates. Nevertheless, this preliminary work has paved the way for a new approach and methodology while raising important questions to be answered. The gold colloidal aggregates were formed near the amyloid fibril-like section of the AD rat hippocampal brain tissues in very minimal frequency in this \sim 55-day old rat, which may progress further in older aged-rats (i.e., > 1 year old mouse or 365 days old rats).

CRediT authorship contribution statement

Kazushige Yokoyama: Conceptualization, Data curation, Formal analysis, Funding acquisition, Investigation, Methodology, Project administration, Resources, Software, Supervision, Validation, Visualization, Writing – original draft, Writing – review & editing. Joshua Thomas: Formal analysis, Writing – review & editing. Windsor Ardner: Formal analysis, Writing – review & editing. Madison Kieft: Formal analysis, Writing – review & editing. Lorenz S. Neuwirth: Conceptualization, Methodology, Project administration, Resources, Supervision, Writing – review & editing. Wei Liu: Formal analysis, Methodology, Writing – review & editing.

Declaration of Competing Interest

The authors declare that there is no conflict of interest.

Data availability

Data will be made available on request.

Acknowledgment

This work was supported by the NSF MRI 2117780. K. Y. is grateful for Geneseo Foundation for the support at the initial stage of this project and Philip Carubia at the Cornell Center for Material Research of Cornell University. The preliminary data for Raman imaging was tested at the Cornell Center for Materials Research shared Facilities which are supported through the NSF MRSEC program (DMR-1719875). M. K. thanks for the SUNY Geneseo Chemistry Department Alumni Summer Research Fellowship (Gerry Rhodes and Kenneth Lipkowitz Fellowship).

Appendix A. Supporting information

Supplementary data associated with this article can be found in the online version at doi:10.1016/j.jneumeth.2023.109892.

References

- Attanasio, F., et al., 2013. Carnosine inhibits $4\beta42$ aggregation by perturbing the H-Bond network in and around the central hydrophobic cluster. ChemBioChem 14, 583–592.
- Bhatia, N.K., Deep, S., 2013. Diagnostic tools dor structural characterization and elucidation of fibrils and their precursors in amyloid fibril formation pathway. J. Proteins Proteom. 4, 149–164.
- Boraschi, D., et al., 2017. Nanoparticles and innate immunity: new perspectives on host defence. Semin. Immunol. 34, 33–51.
- Carey, P.R., 1982. Biochemical Applications of Raman and Resonance Raman Spectroscopies. Academic Press., New York.
- Chung, C.M., Connors, L.H., Benson, M.D., Walsh, M.T., 2001. Biophysical analysis of normal transthyretin: implications for fibril formation in senile systemic amyloidosis. Amyloid J. Protein Fold. Disord. 8.
- Coles, M., Bicknell, W., Watson, A.A., Fairlie, D.P., Craik, D.J., 1998. Solution structure of amyloid beta-peptide(1-40) in a water-micelle environment. is the membranespanning domain where we think it is. Biochemistry 37, 11064–11077.
- Colvin, M.T., et al., 2015. High resolution structural characterization of Ap42 amyloid fibrils by magic angle spinning NMR. J. Am. Chem. Soc. 137, 7509–7518.
- Cook, N.P., Kilpatrick, K., Segatori, L., Martí, A.A., 2012. Detection of α-synuclein amyloidogenic aggregates in vitro and in cells using light-switching
- dipyridophenazine Ruthenium(II) complexes. J. Am. Chem. Soc. 134, 20776–20782. Corbo, C., et al., 2016. The impact of nanoparticle protein corona on cytotoxicity immunotoxicity and target drug delivery. Nanomedicine 11, 81–100.
- Dong, J., et al., 2003. Metal binding and oxidation of Amyloid-beta within isolated senile plaque cores: raman microscopic evidence. Biochemistry 42, 2768–2773.
- El Khoury, Y., et al., 2021. Raman imaging reveals accumulation of hemoproteins in plaques from alzheimer's diseased tissues. ACS Chem. Neurosci. 12, 2940–2945.
- El-Shimy, I.A., Heikal, O.A., Hamdi, N., 2015. Minocycline attenuates Aβ oligomersinduced pro-inflammatory phenotype in primary microglia while enhancing Aβ fibrils phagocytosis. Neurosci. Lett. 609, 36–41.
- Farrera, C., Fadeel, B., 2015. It takes two to tango: understanding the interactions between engineered nanomaterials and the immune system. Eur. J. Pharm. Biopharm. 95 (Part A), 3–12.
- Ferraro, J.R., 1971. Low-Frequency Vibrations of Inorganic and Coordination Compounds. Springer,
- Frydman-Marom, A., Bram, Y., Gazit, E., 2011. Preparation and structural characterization of pre-fibrillar assemblies of amyloidogenic proteins. Non-fibrillar Amyloidogenic Protein Assem. Common Cytotoxins Underlying Degener. Dis. 61–102.
- Galdino, F.E., Picco, A.S., Capeletti, L.B., Bettini, J., Cardoso, M.B., 2021. Inside the protein corona: from binding parameters to unstained hard and soft coronas visualization. Nano Lett. 21, 8250–8257.
- Giacomelli, C.E., Norde, W., 2005. Conformational changes of the amyloid beta-peptide (1-40) adsorbed on solid surfaces. Macromol. Biosci. 5, 401–407.
- Giovanna, C., et al., 2010. Generation of reactive oxygen species by beta amyloid fibrils and oligomers involves different intra/extracellular pathways. Amino Acids 38, 1101–1106.
- Grys, D.-B., de Nijs, B., Salmon, A.R., Huang, J., Wang, W., Chen, W.-H., Scherman, O.A., Baumberg, J.J., 2020. Citrate coordination and bridging of gold nanoparticles: the role of gold adatoms in aunp aging. ACS Nano 14, 8689–8696.
- Guo, T., et al., 2019. Full-scale label-free surface-enhanced Raman scattering analysis of mouse brain using a black phosphorus-based two-dimensional nanoprobe. Appl. Sci. 9, 398–408
- Harada, I., Takeuchi, H., 1986. Raman and ultraviolet resonance Raman spectra of proteins and related compounds. in Spectroscopy of Biological Systems: AdVances in Infrared and Raman Spectroscopy, Vol. 13 (eds. Clark, R.J.H. & Hester, R.E.) 113–175 (Wiley, Chichester, U.K.).
- Heinz, H., et al., 2009. Nature of molecular interactions of peptides with gold, palladium, and Pd-Au bimetal surfaces in aqueous solution. J. Am. Chem. Soc. 131, 9704–9714.
- Heinz, H., Vaia, R.A., Farmer, B.L., Naik, R.R., 2008. Accurate simulation of surfaces and Interfaces of face-centered cubic metals using 12-6 and 9-6 Lennard-Jones potentials. J. Phys. Chem. C 112, 17281–17290.

- Hooshmand, N., Thoutam, A., Anikovskiy, M., Labouta, H.I., El-Sayed, M., 2021. Localized surface plasmon resonance as a tool to study protein corona formation on nanoparticles. J. Phys. Chem. C 125, 24765–24776.
- Huang, W., Xiao, G., Zhang, Y., Min, W., 2021. Research progress and application opportunities of nanoparticle–protein corona complexes. Biomed. Pharmacother. 139, 111541–111559.
- Jankowsky, J.L., et al., 2005. Persistent amyloidosis following suppression of A β production in a transgenic model of Alzheimer disease. PLOS Med. 2, 1318–1333.
- Ji, M., et al., 2018. Label-free imaging of amyloid plaques in Alzheimer's disease with stimulated Raman scattering microscopy. Sci. Adv. 4, 1-8.
- Konduru, N.V., et al., 2017. Protein corona: implications for nanoparticle interactions with pulmonary cells. Part Fibre Toxicol. 14, 42.
- Kowalewski, T., Holtzman, D.M., 1999. In situ atomic force microscopy study of Alzheimer's beta-amyloid peptide on different substrates: new insights into mechanism of beta-sheet formation. Proc. Natl. Acad. Sci. 96, 3688–3693.
- Kusumoto, Y., Lomakin, A., Teplow, D.B., Benedek, G.B., 1998. Temperature dependence of amyloid beta-protein fibrillization. Proc. Natl. Acad. Sci. 95, 12277–12282.
- Langkildea, E.A., Vestergaard, B., 2009. Methods for structural characterization of prefibrillar intermediates and amyloid fibrils. FEBS Lett. 593, 2600–2609.
- Latreille, P.-L., et al., 2022. Scratching the surface of the protein corona: challenging measurements and controversies. ACS Nano 16, 1689–1707.
- Lochocki, B., et al., 2021. Multimodal label-free fluorescence and Raman imaging of amyloid deposits in snap-frozen Alzheimer's disease human brain tissue. Communications Biol. 4, 474–486.
- Lundqvist, M., Sethson, I., Jonsson, B.-H., 2004. Protein adsorption onto silica nanoparticles: conformational changes depend on the particles' curvature and the protein stability. Langmuir 20, 10639–10647.
- Makin, O.S., Serpell, L.C., 2004. Structural characterisation of islet amyloid polypeptide fibrils. J. Mol. Biol. 335, 1279–1288.
- Malmos, K.G., et al., 2017. ThT 101: a primer on the use of thioflavin T to investigate amyloid formation. Amyloid 24, 1–16.
- Mattana, S., Caponi, S., Tamagnini, F., Fioretto, D., Palombo, F., 2017. Viscoelasticity of amyloid plaques in transgenic mouse brain studied by Brillouin microspectroscopy and correlative Raman analysis. J Innov Opt. Health Sci. 10, 1–24.
- Moser, C.C., Page, C.C., Farid, R., Dutton, P.L., 1995. Biological electron transfer. J. Bioenerg. Biomembr. 27, 263–274.
- Muangchuen, A., Chaumpluk, P., Suriyasomboon, A., Ekgasit, S., 2014. Colorimetric detection of Ehrlichia Canis viα nucleic acid hybridization in gold nano-colloids. Sensors 14, 14472–14487.
- Neagu, M., et al., 2017. Protein bio-corona: critical issue in immune nanotoxicology. Arch. Toxicol. 91, 1031–1048.
- Nejadnik, H., et al., 2018. The protein corona around nanoparticles facilitates stem cell labeling for clinical MR imaging. Radiology 286, 938–947.
- Norde, W., 2008. BioInterface Perspective-My voyage of discovery to proteins in flatland. and beyond. Colloids Surf. B Biointerfaces 61, 1–9.
- Overman, S.A., Thomas Jr., G.J., 1999. Raman markers of nonaromatic side chains in an R-helix assembly: Ala, Asp, GGly, Ile, Leu, Lys, Ser, and Val residues of phage fd subunits, lu. Biochemistry 38, 4018–4027.
- Palombo, F., et al., 2018. Detection of Aβ plaque-associated astrogliosis in Alzheimer's disease brain by spectroscopic imaging and immunohistochemistry. Analyst 143, 850–857.
- Politi, J., Spadavecchia, J., Iodice, M., de Stefano, L., 2015. Oligopeptide-heavy metal interaction monitoring by hybrid gold nanoparticle based assay. Analyst 140, 149–155.
- Pujol-Pina, R., et al., 2015. SDS-PAGE analysis of Aβ oligomers is disserving research into Alzheimer's disease: appealing for ESI-IM-MS. Sci. Rep. 5, 14809–14821.
- Rahman, M., Laurent, S., Tawil, N., Yahia, L.H., Mahmoudi, M., 2013. Protein-Nanoparticle Interactions. The Bio-Nano Interface. Springer,, pp. 21–44.
- Rai, S., Kumar, N.S., Singh, H., 2012. A theoretical study on interaction of proline with gold cluster. Bull. Mater. Sci. 35, 291–295.
- Rasheed, P.A., Sandhyarani, N., 2014. Femtomolar level detection of BRCA1 gene using a gold nanoparticle labeled sandwich type DNA sensor. Colloids Surf. B Biointerfaces 1, 7–13.
- Rizevsky, S., Kurouski, D., 2022. Tip-Enhanced Raman Imaging of Photocatalytic processes at the nanoscale. J. Phys. Chem. C 126, 14781–14790.
- Rocha, S., et al., 2005. Adsorption of amyloid beta-peptide at polymer surfaces: a neutron reflectivity study. Chem. Phys. Chem. 6, 2527–2534.
- Sahneh, D.F., Scoglio, C., Riviere, J., 2013. Dynamics of nanoparticleprotein corona complex formation: analytical results from population balance equations (64691-64614). Adv. Sci. 8, e64690 (64691-64614).
- Salvati, A., et al., 2013. Transferrin-functionalized nanoparticles lose their targeting capabilities when a biomolecule corona adsorbs on the surface. Nat. Nanotechnol. 8, 137–143.
- Schladitz, C., Vieira, E.P., Hermel, H., Mohwald, H., 1999. Amyloid-beta-sheet formation at the air-water interface. Biophys. J. 77, 3305–3310.
- Shao, H.Y., Jao, S.C., Ma, K., Zagorski, M.G., 1999. Solution structures of micelle-bound amyloid beta-(1-40) and beta-(1-42) peptides of Alzheimer's disease. J. Mol. Biol. 285, 755–773.

- Smith, J.F., Knowles, T.P.J., Dobson, C.M., MacPhee, C.E., Welland, M.E., 2006. Characterization of the nanoscale properties of individual amyloid fibrils. PNAS 103, 15806–15811.
- Stewart, S., Fredericks, P.M., 1999. Surface-enhanced Raman spectroscopy of peptides and proteins adsorbed on an electrochemically prepared silver surface. Spectrochim. Acta Part A 55, 1615–1640.
- Stiebing, C., et al., 2020. Biochemical characterization of mouse retina of an Alzheimer's disease model by Raman Spectroscopy. ACS Chem. Neurosci. 11, 3301–3308.
- Suarasan, S., Focsan, M., Soritau, O., Maniu, D., Astilean, S., 2015. One-pot, green synthesis of gold nanoparticles by gelatin and investigation of their biological effects on Osteoblast cells. Colloids Surf. B Biointerfaces 32, 122–131.
- Szekeres, G.P., Kneipp, J., 2019. SERS probing of proteins in gold nanoparticle agglomerates. Front. Chem. 7, 1–10.
- Torsten, J., et al., 2018. Impact of nanoparticles on amyloid peptide and protein aggregation: a review with a focus on gold nanoparticles. Nanoscale 10, 20873–21536.
- Venditti, I., et al., 2015. Bioconjugation of gold-polymer core-shell nanoparticles with bovine serum amine oxidase for biomedical applications. Colloids Surf. B Biointerfaces 134, 314–321.
- Walther, M., Plochocka, P., Fischer, B., Helm, H., Uhd Jepsen, P., 2002. Collective vibrational modes in biological molecules investigated by terahertz time-domain spectroscopy. Biopolym. (Biospectroscopy) 67, 310–313.
- Wolfram, J., et al., 2014. The nano-plasma interface: Implications of the protein corona. Colloids Surf. B 124, 17–24.
- Yokoyama, K. Investigation of protein-protein interaction utilizing nano-gold colloid surface: Application to SARS CoV-2 spike protein coated gold colloids. in *Physical Chemistry Research at Undergraduate Institutions* (eds. Hopkins, T. & Parish, C.A.) (ACS Books, submitted for publication).
- Yokoyama, K. Protein Corona Formation and Aggregation Process of Amyloid beta 1–40 Coated Gold Nano-Colloids. *Langmuir* (To be submitted for publication).
- Yokoyama, K., et al. In situ SERS study of the Hippocampus of Alzheimer's disease rat (in preparation).
- Yokoyama, K., et al., 2008. Nanoscale size dependence in the conjugation of amyloid beta and ovalbumin proteins on the surface of gold colloidal particles. Nanotechnology 19, 375101–375108.
- Yokoyama, K., et al., 2009. Microscopic investigation of reversible nanoscale surface size dependent protein conjugation. Int. J. Mol. Sci. 10, 2348–2366.
- Yokoyama, K., 2010. In: Chen, E.J., Peng, N. (Eds.), Nanoscale protein conjugation in Advances in Nanotechnology. Nova Science Publishing, pp. 65–104.
- Yokoyama, K., 2011a. Modeling of reversible protein conjugation on nanoscale surface. In: Musa, S.M. (Ed.), Computational Nanotechnology: Modeling and Applications with MATLAB. CRC Press, pp. 381–409.
- Yokoyama, K., 2011b. Description of Solvent-Dependent and Nanoscale Diffusion Process in Silica Based Sol-gel Matrix. In: Morris, R.E. (Ed.), The Sol-gel Process Uniformity, Polymers and Applications. Nova Science Publishers, Inc, New York, pp. 371–398.
- Yokoyama, K., 2012. Nano size dependent properties of colloidal surfaces. In: Ray, P.C. (Ed.), Colloids: Classification, Properties and Applications. Nova Publishers, pp. 25–58.
- Yokoyama, K., 2013. Controlling Reversible Self Assembly Path of Amyloid Beta Peptide over Gold Colloidal nanoparticle's Surface. In: Musa, S.M. (Ed.), Nanoscale Spectroscopy with Applications. CRC Press-Taylor and Francis Group, LLC, pp. 279–304.
- Yokoyama, K., et al., 2019. Examination of adsorption orientation of amyloidogenic peptides over nano-gold colloidal particles' surfaces. Int. J. Mol. Sci. 20, 5354–5380.
- Yokoyama, K., Welchons, D.R., 2007. The conjugation of amyloid beta protein on the gold colloidal nanoparticles' surfaces. Nanotechnology 18, 105101–105107.
- Yokoyama, K., Gaulin, N.B., Cho, H., Briglio, N.M., 2010. Temperature dependence of conjugation of amyloid beta peptide on the gold colloidal nanoparticles. J. Phys. Chem. A 114, 1521–1528.
- Yokoyama, K., Catalfamo, C.D., Yuan, M., 2015. Reversible peptide oligomerization over nanosclae gold surfaces. AIMS Biophys. 2, 679–695.
- Yokoyama, K. & Kieft, M. Investigation by SERS on nano-size dependent peptide-peptide interaction over gold colloidal surface (to be submitted for publication).
- Yokoyama, K., Thomas, J., Ardner, W., Neuwirth, L.S., Liu, W., 2022. Method for in situ detection of amyloid formation in the hippocampus of the Cohen's Alzheimer's disease rat model by Surface Enhanced Raman Scattering. in SSRN (https://papers.ssrn.com/sol3/papers.cfm?abstract_id=4092650).
- Yu, X., et al., 2018. Surface enhanced Raman spectroscopy distinguishes amyloid betaprotein isoforms and conformational states. Protein Sci. 27, 1427–1438.
- Zhao, T., et al., 2014. Gold nanorod enhanced two-photon excitation fluorescence of photosensitizers for two-photon imaging and photodynamic therapy. ACS Appl. Mater. Interfaces 6, 2700–2708.
- Zhdanov, V.P., Kasemo, B., 1998. Monte Carlo simulation of the kinetics of protein adsorption. Protein. Struct. Funct. Genet 30, 177–182.
- Zurdo, J.J., Guijarro, I., Dobson, C.M., 2001. Preparation and characterization of purified amyloid fibrils. J. Am. Chem. Soc. 123, 8141–8142.